Journal of Materials Chemistry A

Fe$_2$O$_3$@SnO$_2$ nanoparticle decorated graphene flexible films as high-performance anode materials for lithium-ion batteries†

Shuo Liu, Ronghua Wang, Miaomiao Liu, Jianqiang Luo, Xihai Jin,* Jing Sun* and Lian Gao

A flexible graphene film decorated with spindle-like Fe$_2$O$_3$@SnO$_2$ nanoparticles was fabricated through vacuum filtration of Fe$_2$O$_3$@SnO$_2$ and GO mixing solution, followed by thermal reduction. The core–shell structured Fe$_2$O$_3$@SnO$_2$ nanoparticles were synthesized through a facile hydrothermal route, which avoided agglomeration of Fe$_2$O$_3$ and SnO$_2$ nanoparticles and was beneficial for electrolyte diffusion. Microstructure characterizations showed that the spindle-like Fe$_2$O$_3$@SnO$_2$ nanoparticles were uniformly dispersed between layered graphene nanosheets, forming a sandwich-like structure. The unique interleaved structure was favorable for lithium ion diffusion and electron transfer. As binder-free electrodes for lithium-ion batteries, the flexible Fe$_2$O$_3$@SnO$_2$/GS films exhibited discharge and charge capacities of 2063 and 1255 mA h g^{-1} respectively, with an excellent cycling performance of 1015 mA h g^{-1} even after 200 cycles. The specific capacity of the Fe$_2$O$_3$@SnO$_2$/GS electrode is higher than that of both Fe$_2$O$_3$/GS and SnO$_2$/GS electrodes, indicating a positive synergistic effect of Fe$_2$O$_3$ and SnO$_2$ on the improvement of electrochemical performance.

Introduction

With the rapid development of portable electronics and hybrid electric vehicles, high performance electric energy storage devices are urgently needed.[1–5] Lithium-ion batteries have attracted worldwide attention as dominant energy storage devices due to their convenience in operation, but they suffer from limited gravimetric capacity of the electrode materials. For instance, the gravimetric capacity of a standard commercialized carbon-based anode material is only about 372 mA h g^{-1}, which cannot meet the demand for high efficiency energy storage. In recent decades, transition-metal oxides, such as Co$_3$O$_4$,[6] Fe$_2$O$_3$,[7] MnO$_2$ (ref. 8) and SnO$_2$ (ref. 9), have received tremendous interest as anode materials for lithium-ion batteries due to their high theoretical specific capacity. Among these materials, Fe$_2$O$_3$ is especially attractive because of its abundance in natural resources and low cost. However, just like other transition-metal oxide electrode materials, the tremendous volume change associated with Li-ion insertion/extraction often leads to the pulverization and subsequent fall off of the active material from the electrode, resulting in significant capacity fading.

Although the use of nanosized materials can effectively accommodate the volume change induced strain and to some extent alleviate this problem, capacity fading is still inevitable in long term cycling, because of the electrochemical aggregation effect of the nanoparticles. This together with the poor electrical conductivity of the material seriously limits the cyclability and rate performance improvement of the electrode, being the major drawback to hinder its practical application.

In order to address the above issues, several strategies have been proposed. One strategy is to combine Fe$_2$O$_3$ with other metal oxides to form hybrid nanostructures, such as Fe$_2$O$_3$@SnO$_2$ nanocapsules,[10] Co$_3$O$_4$/Fe$_2$O$_3$ nanowires,[11,12] Fe$_2$O$_3$@NiO nanorods[13] and TiO$_2$@Fe$_2$O$_3$ nanoarrays.[14,15] The formation of such hybrid nanostructures can effectively prevent Fe$_2$O$_3$ nanoparticles from electrochemical aggregation, shorten the Li$^+$ insertion/extraction pathways[11,16,17] and well accommodate the strain accompanied by volume change. Many studies indicated that the synergistic effects of the above factors can lead to a significant improvement in cyclability and capacity of the material.

Another strategy for the improvement of the electrochemical performance of Fe$_2$O$_3$ is to integrate it with an electrically conducting matrix such as amorphous carbon,[18–20] graphene[21,22] or carbon nanotubes (CNTs)[23,24] to enhance the structural stability and electric conductivity of the electrode. Particularly, graphene is an ideal electrically conducting matrix, owing to its high theoretical specific area, excellent electronic conductivity and remarkable mechanical flexibility.[25–28] Nowadays, the

The State Key Lab of High Performance Ceramics and Superfine Microstructure, Shanghai Institute of Ceramics, Chinese Academy of Sciences, 1295 Dingxi Road, Shanghai 200050, P.R. China. E-mail: jinxihai@hotmail.com; jingsun@mail.sic.ac.cn; Fax: +86-21-52413122; Tel: +86-21-52414301

integration of graphene with transition metal oxides for use as a Li-ion battery electrode has been intensively studied with many promising results.[6,29–35] Ruoff and Guo found that a rational combination of graphene with Fe_2O_3 could greatly improve the electrical conductivity and structural stability of the electrode, leading to significant improvement in its electrochemical performances.[36,37] What is more interesting is that due to the high aspect ratio and mechanical flexibility of graphene, the graphene/transition metal oxide hybrid materials can be made into free-standing films and directly used as Li-ion battery electrodes.[38–42] In comparison with conventional electrodes with metal current collectors, such electrodes show much reduced weight, which is very helpful for increasing the capacity to weight ratio of the electrode.

In the present work, a Li-ion battery anode based on core–shell structured $Fe_2O_3@SnO_2$ hybrid nanoparticle decorated graphene films was designed through a combination of the above two strategies. We hope that the combination of nano-particle hybridization and graphene incorporation may result in a synergistic effect in further improving the electrical performance of the material. According to this design concept, free-standing $Fe_2O_3@SnO_2/GS$ film electrodes were prepared by vacuum filtration of $Fe_2O_3@SnO_2$ spindle-like nanoparticles and graphene oxide (GO) mixing solution, followed by thermal reduction. It was found that the spindle-like $Fe_2O_3@SnO_2$ nanoparticles were uniformly distributed among graphene sheet (GS) layers, forming a sandwich-like structure. Due to the strong interaction between the SnO_2 shell and the Fe_2O_3 core as well as the GS conductivity enhancing agent, the electrochemical performance of the electrode was remarkably improved. It showed a high stable capacity of more than 1000 mA h g^{-1} over 200 charge–discharge cycles along with good rate capability.

Experimental

Material synthesis

All chemicals used were of analytical grade without further purification. The fabrication process involves: (1) synthesis of $FeOOH@SnO_2$ nanospindles and (2) fabrication of $Fe_2O_3@SnO_2/GS$ films.

Synthesis of $FeOOH@SnO_2$. A nanospindle-like FeOOH precursor was synthesized based on a previously reported hydrolysis method.[43] A SnO_2 porous shell was coated on the surface of FeOOH by a simple surfactant-free hydrothermal method. Specifically, 0.085 g FeOOH was dispersed in a mixing solution of 20 mL distilled water and 30 mL ethanol, then 0.115 g $Na_2SnO_3 \cdot 4H_2O$ and 0.75 g urea were successively added. After ultrasonicating for an hour, the resulting solution was transferred into a Teflon-lined stainless steel autoclave and kept at 170 °C for 36 h, and then cooled down to room temperature. The resulting $FeOOH@SnO_2$ nanoparticles were collected by centrifugation, washed with distilled water and dried at 50 °C for 4 h in a vacuum.

Fabrication of $Fe_2O_3@SnO_2/GS$ films. Aqueous GO solution with GO concentration of 0.9 wt% was prepared by a modified Hummer's method.[44] $FeOOH@SnO_2$ solution was prepared by dispersing $FeOOH@SnO_2$ into water. With the aid of magnetic

stirring, an appropriate amount of GO solution was added into the $FeOOH@SnO_2$ solution to form a mixing solution, which was further dispersed through ultrasonication for 5 minutes using a Sonifier (SK250HP, 52 Hz). Afterwards, 15 mL of the mixing solution was vacuum filtered using inorganic filter paper with a pore diameter of 220 nm. The deposit was dried and peeled off from the filter paper to get a $FeOOH@SnO_2/GO$ film. Finally, the film was annealed at 500 °C in Ar flow for 2 h to convert it into a $Fe_2O_3@SnO_2/GS$ film. To optimize the electro-chemical performance of the film, the mass proportion of graphene in the film was controlled at ~40%. For comparison, Fe_2O_3/GS and SnO_2/GS films were also fabricated by replacing $FeOOH@SnO_2$ with FeOOH and SnO_2, respectively, according to the same fabrication procedure above.

Characterization

Morphologies of samples were characterized by scanning electron microscopy (SEM, JSM-6700F) at an acceleration voltage of 10.0 kV. Transmission electron microscopy (TEM, JEM-2100F, JEOL, Tokyo, Japan) was operated at an acceleration voltage of 200 keV. X-ray diffraction (XRD) was carried out on a D/max 2550 V diffractometer with Cu-Kα irradiation at λ = 1.5406 Å. Thermal gravimetric analysis (TGA) was conducted in air using Du Pont Instruments TGA 2950 from room temperature to 800 °C with a heating rate of 10 °C min^{-1}. Raman spectroscopy was recorded on a DXR Raman Microscope with a 532 nm excitation length, Thermal Scientific Corporation, USA. X-ray photoelectron spectroscopy (XPS) analysis was conducted in the region of 0–1200 eV using a Mg Kα (1253.6 eV) monochromatic X-ray source (Axis Ultra DLD, Kratos). N_2 adsorption/desorption isotherms were determined using a Micromeritics ASAP2010 Analyzer (USA).

Electrochemical measurements

The synthesized $Fe_2O_3@SnO_2/GS$ films were directly used as working electrodes without any binder and additive. For electrochemical performance testing, the $Fe_2O_3@SnO_2/GS$ films were dried in a vacuum at 120 °C for 2 h and assembled into CR 2025 type coin cells with lithium metal as counter electrodes. Mass loading of the film electrode was controlled at about ~1.9 mg cm^{-2}, including graphene and the metal oxides. The specific capacity was calculated based on the total mass of the electrode. Cyclic voltammetry (CV) was carried out in the voltage range of 0–3.0 V with a scan rate of 0.5 mV s^{-1}. The galvanostatic discharge–charge was characterized on a CT2001 battery tester. Electrochemical impedance spectroscopy (EIS) measurements of cells were performed on a CHI660D electrochemical work-station with a sine wave of 5 mV over a frequency range of 100 kHz to 0.01 Hz. Cells were assembled in an Ar-filled glove-box with concentrations of moisture and oxygen below 1.0 ppm. The electrolyte used was $LiPF_6$ (1.0 M) in a mixture of ethylene carbonate and diethyl carbonate (1 : 1 by volume).

Results and discussion

Fig. 1 shows the SEM and TEM images of the FeOOH and $FeOOH@SnO_2$ nanoparticles. The FeOOH nanoparticles were
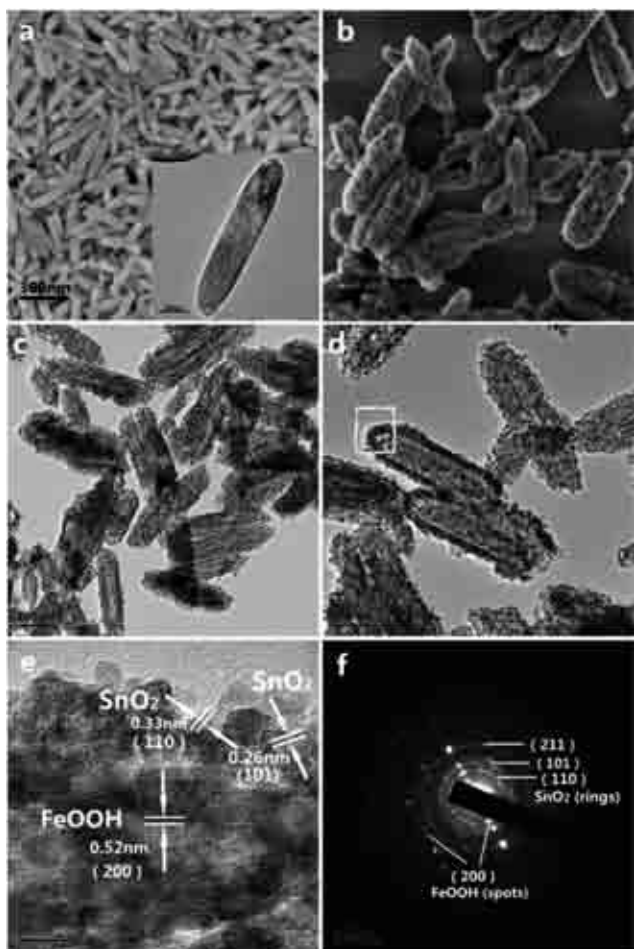
Fig. 1 (a) SEM image of FeOOH nanoparticle; the inset in (a) corresponds to the TEM image of FeOOH. (b) SEM image of FeOOH@SnO$_2$; (c) TEM image of FeOOH@SnO$_2$; (d) magnified TEM image of FeOOH@SnO$_2$; (e) HRTEM image of FeOOH@SnO$_2$; (f) SAED pattern of FeOOH@SnO$_2$.

spindle-like in morphology and highly dispersed (Fig. 1a). The diameter and length of the nanospindles were about 40–70 nm and 200–400 nm, respectively. After hydrothermal treatment in Na$_2$SnO$_3$ and urea mixing solution, the SnO$_2$ layer of 10–12 nm thickness was uniformly coated on the FeOOH particle surface, forming a core-shelled structure. The core–shell structured FeOOH@SnO$_2$ nanoparticle well inherited the spindle-like morphology of FeOOH (Fig. 1b). However, its specific surface area (96 m^2 g^{-1}) showed a great increase over that of FeOOH (39 m^2 g^{-1}, Fig. S1, ESI†), because of the coating of extremely fine SnO$_2$ nanoparticles on its surface, which were less than 5 nm in size.

In order to acquire deep understanding of the microstructure of the core-shelled FeOOH@SnO$_2$ nanoparticles, high resolution TEM (HRTEM) and selected area electron diffraction (SAED) were conducted in the core–shell interface region marked by a square in Fig. 1d. The HRTEM image is shown in Fig. 1e. For the core, only one kind of lattice fringe could be observed and the typical spacing of the adjacent lattice planes was 0.52 nm, corresponding to the (200) crystal plane of FeOOH.

For the shell, two kinds of lattice fringes with interplanar spacings of 0.33 nm and 0.26 nm were observed, which were in good accordance with the (110) and (101) crystal planes of tetragonal SnO$_2$. The corresponding selected area electron diffraction of the core–shell interface region showed two sets of diffraction patterns formed by bright diffraction spots and diffraction rings, respectively. The sharp diffraction spots were attributed to the spindle FeOOH, while the bright diffraction rings originated from SnO$_2$ nanoparticles. Both the HRTEM and SAED results indicated good crystallinity of the core-shelled FeOOH@SnO$_2$ nanoparticle in the whole, with the FeOOH core being a single crystal in nature.

Based on the successful synthesis of FeOOH@SnO$_2$ nanospindles, two dimensional Fe$_2$O$_3$@SnO$_2$/GS films were fabricated according to the fabrication procedure illustrated in Scheme 1. In brief, the FeOOH@SnO$_2$ nanospindles were mixed with GO solution, and vacuum-filtered to obtain a flexible freestanding FeOOH@SnO$_2$/GO film. Finally, the FeOOH@SnO$_2$/GO was reduced to Fe$_2$O$_3$@SnO$_2$/GS by a simple annealing treatment. Owning to the outstanding dispersibility of FeOOH@SnO$_2$ nanoparticles in GO solution (Fig. S2†), flexible Fe$_2$O$_3$@SnO$_2$/GS films could be successfully obtained, and the spindle-like morphology of FeOOH@SnO$_2$ nanoparticles allowed for their proper orientation in the graphene films.[45]

The phase assemblages of the products before and after thermal reduction were characterized by XRD (Fig. 2). As expected, the tetragonal FeOOH (JCPDS 75-1594) transformed to Fe$_2$O$_3$ (JCPDS 33-0664) after the annealing process, whereas the crystal structure of SnO$_2$ nanoparticles remained unchanged (tetragonal, JCPDS 71-0652). Importantly, no diffraction peak characteristic of restacked graphene nanosheets was found at about 25°, indicating the uniform dispersion of graphene nanosheets in the 2D film. SEM cross-section views and top views (Fig. 3) of the Fe$_2$O$_3$@SnO$_2$/GS film showed that the spindle-like morphology of FeOOH@SnO$_2$ nanoparticles was well preserved after its reduction to Fe$_2$O$_3$@SnO$_2$, as also demonstrated by TEM images in Fig. S3a and b.† The

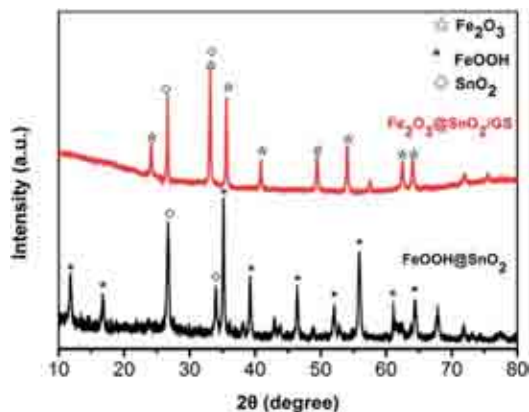**Scheme 1** Schematic illustration of the synthesis process of the Fe$_2$O$_3$@SnO$_2$/GS film.

Fig. 2 XRD pattern of FeOOH@SnO_2 nanoparticles and Fe_2O_3@SnO_2/GS films.

Fig. 4 (a) XPS spectra and (b) C 1s spectra of FeOOH@SnO_2/GO and Fe_2O_3@SnO_2/GS films; (c) Raman spectra of GS and Fe_2O_3@SnO_2/GS films; (d) TGA curve of the Fe_2O_3@SnO_2/GS film.

Fe_2O_3@SnO_2/GS film took a sandwich-like structure and was about 14 μm in thickness. Fe_2O_3@SnO_2 particles were uniformly embedded within the graphene layers and hereby expanded the interspacing of neighboring graphene layers. Such a structure was helpful for preventing graphene layers from agglomeration and would greatly facilitate electrolyte diffusion when it was used as an anode in Li-ion batteries.

For comparison, Fe_2O_3/GS films and SnO_2/GS films were also fabricated as shown in Fig. S4.† Similar to the Fe_2O_3@SnO_2/GS film, these two films also possessed a sandwich-like structure consisting of GS and metal oxide particles. However, the metal oxide particle morphologies in the latter films showed a great difference in comparison with the former. It seems that a strong interaction between Fe_2O_3 and SnO_2 nanoparticles exists in controlling their morphologies. The SnO_2 coating on FeOOH particle surface showed a stabilizing effect on the spindle-like morphology of FeOOH when it was reduced to Fe_2O_3. Without this coating, the FeOOH particles were reduced to Fe_2O_3 cubics in Fe_2O_3/GS films. On the other hand, the SnO_2 nanoparticles in the SnO_2/GS film showed a significant increase in agglomeration without the dispersing effect of the FeOOH core.
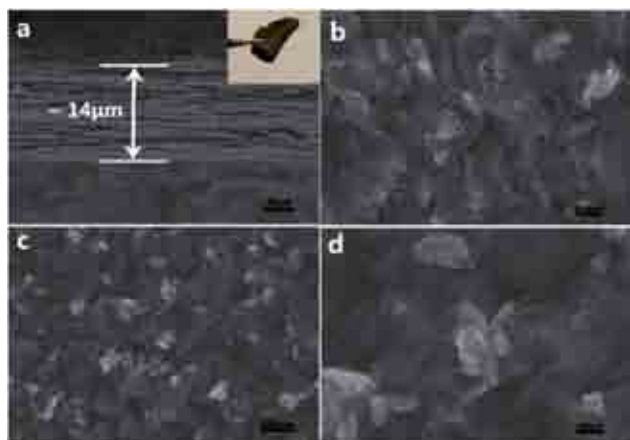
Fig. 4a shows the X-ray photoelectron spectrum (XPS) of the Fe_2O_3@SnO_2/GS and FeOOH@SnO_2/GO films. The peaks at 710.7, 725.8, 487and 495.6 eV in the XPS spectrum of the Fe_2O_3@SnO_2/GS film were ascribed to the Fe $2p_{3/2}$, Fe $2p_{1/2}$, Sn $3d_{5/2}$ and Sn $3d_{3/2}$ spinning of Fe_2O_3 and SnO_2, respectively.[24,37,46] The chemical changes in GO before and after thermal reduction could be deduced from the changes in the C 1s spectrum of FeOOH@SnO_2/GO and Fe_2O_3@SnO_2/GS films (Fig. 4b). According to the literature,[26,47] five kinds of carbon belonging to C(O)–O, C=O, C–O–C, C–OH and C=C can be detected, and their binding energies are indicated by dashed vertical lines in Fig. 4b. A comparison between the C 1s spectrum of FeOOH@SnO_2/GO and Fe_2O_3@SnO_2/GS films found a sharp decrease in the oxygen-containing functional groups in the latter sample. Accordingly, the atomic ratio of carbon and oxygen (C/O) increased from 3.21 for FeOOH@SnO_2/GO to 7.23 for Fe_2O_3@SnO_2/GS, demonstrating a deep reduction of GO.

Moreover, the Raman spectrum of the Fe_2O_3@SnO_2/GS film showed a red shift of the G band of graphene from 1590 cm^{-1} to 1594 cm^{-1} in comparison with that of the bare GS film, indicating an n-type doping effect of Fe_2O_3@SnO_2 particles on GS.[48,49] Such an electron donating effect might result from the interaction between the nanoparticles and GS, which would contribute a lot in improving the electrochemical performance. Thermogravity (TG) analysis of the Fe_2O_3@SnO_2/GS film showed a weight loss of 35.5% at temperature range above 580 °C, which was mainly caused by the combustion of GS in air. On this basis, the weight content of Fe_2O_3@SnO_2 in the film could be determined to be around 64.5%.

The Fe_2O_3@SnO_2/GS film was flexible and mechanically robust, and could be folded and twisted without breaking. This plus the good electron transport properties endowed by the graphene layers enabled it to serve as a self-supporting electrode. Fig. 5a shows the cyclic voltammetry (CV) behavior of the Fe_2O_3@SnO_2/GS film electrode measured in the potential range of 0–3.0 V at a scan rate of 0.5 mV s^{-1}. The CV behavior of the

Fig. 3 Cross-section (a and b) and top-view SEM images (c and d) of a Fe_2O_3@SnO_2/GS film; the inset in (a) is a digital photograph of a Fe_2O_3@SnO_2/GS film showing good flexibility.
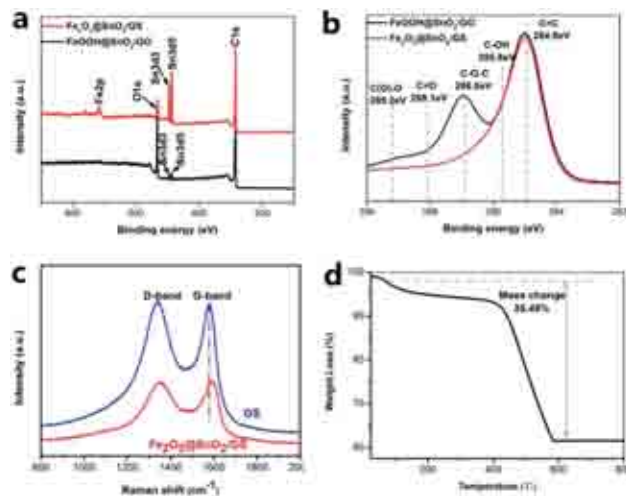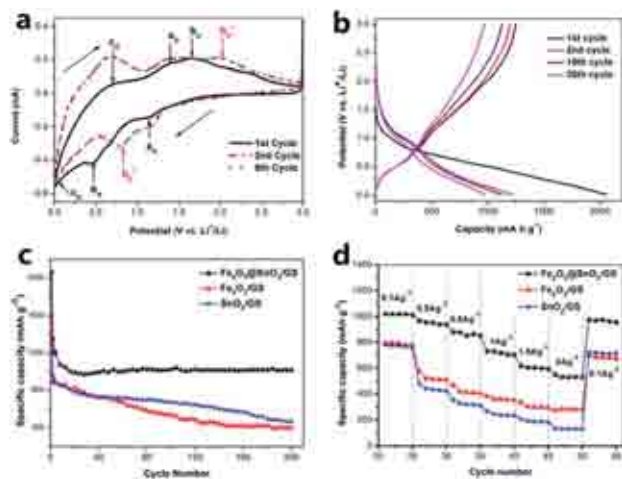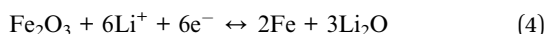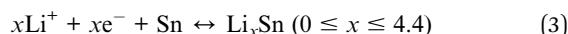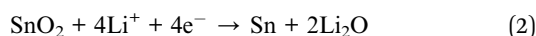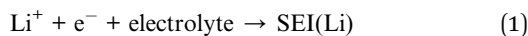
Fig. 5 (a) Cyclic voltammograms of the Fe$_2$O$_3$@SnO$_2$/GS film anode at a scan rate of 0.5 mV s^{-1} over a potential range of 0–3.0 V vs. Li$^+$/Li; (b) charge–discharge profiles of the Fe$_2$O$_3$@SnO$_2$/GS film anode at a current density of 100 mA g^{-1}; (c) cycling performance of the different electrodes at a current density of 100 mA g^{-1}; (d) rate capability of the different electrodes at various current densities.

Fe$_2$O$_3$@SnO$_2$/GS anode is closely analogous to a combination of the CV behaviors of Fe$_2$O$_3$/GS and SnO$_2$/GS (Fig. S4†), which are generally consistent with the reports in the literature.[50,51] In the first cathodic scan, three reduction peaks, denoted as peak a$_R$, b$_R$ and c$_R$, are observed at about 1.2, 0.45 and 0.06 V, respectively. The broad reduction peak a$_R$ can be ascribed to the formation of Solid Electrolyte Interphase (SEI, eqn (1)) and reduction of SnO$_2$ to Sn (eqn (2)).[52,53,55] The other two characteristic peaks c$_R$ and b$_R$ can be associated with the reversible reaction of Sn and Li$^+$ forming Li$_x$Sn alloys (eqn (3)),[54] and the reduction of Fe^{3+} to Fe^0 by Li (eqn (4))[55] respectively.

$$Li^+ + e^- + electrolyte \rightarrow SEI(Li) \tag{1}$$

$$SnO_2 + 4Li^+ + 4e^- \rightarrow Sn + 2Li_2O \tag{2}$$

$$xLi^+ + xe^- + Sn \leftrightarrow Li_xSn \ (0 \leq x \leq 4.4) \tag{3}$$

$$Fe_2O_3 + 6Li^+ + 6e^- \leftrightarrow 2Fe + 3Li_2O \tag{4}$$

Corresponding to the above reduction peaks, three oxidation peaks appeared in the first anodic scan. The oxidation peak a$_O$ at ~1.3 V is thought to be likely resulted from a partial reversibility of reaction (2),[54] although it is generally acknowledged that reactions (1) and (2) are irreversible and often lead to a large irreversible capacity loss in the first cycle. As to the oxidation peaks b$_O$ and c$_O$ at ~1.65 V and ~0.75 V, they can be attributed to the oxidation of Fe^0 to Fe^{3+} and the dealloying process of Li$_x$Sn.[21,53]

Furthermore, it is observed from the initial five CV cycles that there is substantial difference between the first and subsequent cycles. Particularly, the peaks b$_R$ and b$_O$ in the first cycle shifted to b$_R'$ and b$_O'$ in the subsequent cycles, suggesting the occurrence of structure and electrochemical property

variation in the electrode,[56] while in the subsequent cycles, the CV curves became almost completely overlapped, indicating that the structure and electrical properties of the electrode became relatively stable. At this time, reactions (3) and (4) were the main reactions that contributed to the capacity of the electrode because of their high reversibility.

The galvanostatic charge and discharge of the electrode were evaluated at a current density of 100 mA g^{-1} between 0.01 and 3.0 V vs. Li$^+$/Li. As shown in Fig. 5b, the nonlinear multi-plateau nature of the charge–discharge curves coincides well with the CV results, and are closely related to the occurrence of multistep intercalation/deintercalation of lithium-ions in the electrode.[36] The first cycle discharge and charge capacities reached respective values of 2063 and 1255 mA h g^{-1}, much higher than the theoretical capacities of Fe$_2$O$_3$ (1007 mA h g^{-1}), SnO$_2$ (782 mA h g^{-1}) and graphene (372 mA h g^{-1}). Although a big capacity loss of 39.1% occurred in the first cycle because of the SEI film formation and the irreversible reactions of lithium ions with oxygen-containing functional groups on the graphene surface,[57] the capacity loss narrowed hereafter. After 30 charge–discharge cycles, the discharge capacity still remained up to 980.8 mA h g^{-1}. It is believed that the high capacity should be associated with the large surface area of the electrode with more active sites for Li storage, which were mainly nanosized Sn and Fe$_2$O$_3$. Although graphene in the electrode could also contribute to the capacity, this contribution was nearly negligible in comparison with that of Sn and Fe$_2$O$_3$ nanoparticles. Galvanostatic charge–discharge measurement of the bare graphene electrode found a very low capacity of about 67 mA h g^{-1} after 5 cycles (Fig. S6†), which was much lower than that of the Fe$_2$O$_3$@SnO$_2$/GS electrode.[41,42]

Fig. 5c shows the cycling performance of the Fe$_2$O$_3$@SnO$_2$/GS electrode along with those of Fe$_2$O$_3$/GS and SnO$_2$/GS electrodes at a current rate of 100 mA g^{-1}. Generally, the capacity loss caused by the irreversible Li insertion process and the strain induced pulverization and subsequent fall-off of active materials from the current collector can be observed in lithium-ion batteries after long term cycling. However, benefiting from the unique core-shelled morphology of Fe$_2$O$_3$@SnO$_2$ nanoparticles, the electrochemical agglomeration and growth of Fe$_2$O$_3$ and Sn metallic particles during cycling can be effectively retarded. This well accommodated the strain induced by Li-ion insertion and extraction, and made the active material particles more resistant to strain induced pulverization, rendering the Fe$_2$O$_3$@SnO$_2$/GS electrode with excellent cyclability. Obvious capacity loss with cycling was only observed in the first 20 cycles, afterwards the capacity became stable at about 1000 mA h g^{-1}. In comparison with the Fe$_2$O$_3$/GS and SnO$_2$/GS electrodes, the Fe$_2$O$_3$@SnO$_2$/GS electrode showed great superiority not only in capacity but also cyclability. The first cycle discharge capacities of the Fe$_2$O$_3$/GS and SnO$_2$/GS electrodes were about 1620 mA h g^{-1} and 1344 mA h g^{-1}, respectively (Fig. 5c). Upon further cycling, the capacities of these electrodes declined rapidly. After 200 cycles, the Fe$_2$O$_3$/GS and SnO$_2$/GS electrodes showed respective capacity of 401.2 mA h g^{-1} and 468.5 mA h g^{-1}, which were less than half of the remnant capacity of the Fe$_2$O$_3$@SnO$_2$/GS electrode (1015 mA h g^{-1}), despite that the active material loadings of these electrodes were nearly the same (Fig. S7†).

Fig. 5d shows the rate capabilities of the electrodes, which were measured after the electrodes were activated through galvanostatic cycling at 0.1 A g^{-1} for 20 cycles to make their electrical performance relatively stable. The Fe_2O_3@SnO_2/GS electrode exhibits reversible capacities of 1019, 955, 720, 605 and 535 mA h g^{-1} at current densities of 0.1, 0.5, 1, 1.5 and 2 A g^{-1}, respectively. The capacity retention was up to 53% when the current density was increased by twenty fold from 0.1 to 2 A g^{-1}. In contrast, under the same conditions, the Fe_2O_3/GS and SnO_2/GS electrodes showed respective capacity retention of 35% and 17%. The rate capability of the Fe_2O_3@SnO_2/GS electrode was much improved over that of the other two electrodes, which was mainly attributed to enhanced electrochemical reaction kinetics of the electrode.

To gain insight into the electrochemical reaction kinetics of different electrodes, electrochemical impedance spectra of samples measured and are given in Fig. 6a–b in the form of the Nyquist plot. The impedance spectrum of each sample is comprised of one compressed semicircle in the high-frequency region and a straight line in the low frequency region. The impedance data were fitted using an equivalent electrical circuit shown as the inset in Fig. 6a, where R_s stands for bulk resistance of the electrochemical system, R_{ct} for the charge transfer resistance, CPE for the constant phase element and W_o for the Warburg impedance of electrolyte ion diffusion behavior.[37,58] The formation of SEI films during cycling as shown in Fig. 6c–d hindered charge transfer speed, and caused an increase in R_{ct} of the Fe_2O_3/GS electrode (Fig. S8†). However, benefiting from the formation of metallic Sn on the electrolyte/Fe_2O_3 interface, which enhanced the electronic conductivity, the R_{ct} of Fe_2O_3@SnO_2/GS electrode was found to be significantly reduced from 34.31 to 22.57 Ω after 10 cycles of charge and discharge (Fig. 6a). Actually, the Fe_2O_3@SnO_2/GS electrode showed the

lowest post-cycling charge transfer resistance (R_{ct} = 22.57 Ω) compared with the Fe_2O_3/GS electrode (R_{ct} = 66.54 Ω) and SnO_2/GS electrode (R_{ct} = 41.46 Ω). This would facilitate rapid charge transfer and result in improved electrochemical reaction kinetics and rate capability of the electrode. In addition, it is worth noting that aside from the enhanced electronic conductivity, the electrochemical agglomeration retarding effect of the unique core-shelled Fe_2O_3@SnO_2 nanoparticles and the highly porous structure of the total electrode can also contribute to the improved electrochemical reaction kinetics by providing more active sites for Li storage and rapid channel for electrolyte diffusion, resulting in not only better cyclability but enhanced rate capability as well.

Finally, SEM observation indicated that the electrode showed good stability. Except the formation of SEI films on the graphene sheet surface, no obvious change in its microstructure occurred even after charge and discharge for 50 cycles. This good structural stability could partially account for the superior cyclability of the electrode.

Conclusions

In summary, free-standing graphene films decorated with Fe_2O_3@SnO_2 nanoparticles were successfully fabricated for use as Li-ion battery anodes. The electrode showed a sandwich-like structure with core–shell structured Fe_2O_3@SnO_2 nanoparticles homogenously attached on graphene layers. Due to the synergistic effect of Fe_2O_3 and SnO_2 on retarding electrochemical aggregation of the nanoparticles, as well as the good electronic conductivity and rapid electrolyte diffusion channel provided by the three-dimensional interconnected porous graphene networks, this electrode showed great improvement in capacity, cyclability and rate capability over the Fe_2O_3/GS and SnO_2/GS electrodes. Although significant capacity fading was observed in the initial stage of cycling, owning to the occurrence of irreversible lithium storage reactions in it, the capacity became stable at about 1000 mA h g^{-1} after charging and discharging for 20 cycles. A high reversible discharge capacity of 1015 mA h g^{-1} still remained at the 200th cycle, which was almost over two times the remnant capacity of Fe_2O_3/GS and SnO_2/GS electrodes.

Acknowledgements

Fig. 6 (a) EIS spectra of the Fe_2O_3@SnO_2/GS electrode before and after ten cycles of charge−discharge; (b) EIS spectra of all the three electrodes after ten cycles of charge−discharge; (c–d) SEM images of the Fe_2O_3@SnO_2/GS film after 50 cycles of discharge−charge. The solid lines in (a) and (b) represent the fitting results of EIS spectra using an equivalent circuit shown as the inset in (a). All the cells are charged and discharged at a current density of 100 mA g^{-1}. The geometrical surface areas of the electrodes used in these cells are all about 1 cm^2.

Notes and references

1 A. L. M. Reddy, S. R. Gowda, M. M. Shaijumon and P. M. Ajayan, *Adv. Mater.*, 2012, **24**, 5045–5064.

2 G. Wang, L. Zhang and J. Zhang, *Chem. Soc. Rev.*, 2012, **41**, 797–828.

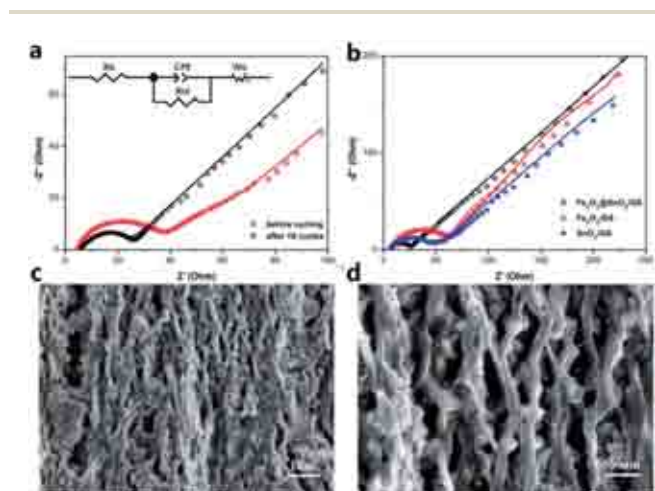3 J. Jiang, Y. Li, J. Liu, X. Huang, C. Yuan and X. W. D. Lou, *Adv. Mater.*, 2012, **24**, 5166–5180.

This journal is © The Royal Society of Chemistry 2014

J. Mater. Chem. A, 2014, **2**, 4598–4604 | **4603**

4 J. Liu and X. Liu, *Adv. Mater.*, 2012, **24**, 4097–4111.

5 Y. Zhou, M. Xue and Z. Fu, *J. Power Sources*, 2013, **234**, 310–332.

6 Z.-S. Wu, W. Ren, L. Wen, L. Gao and J. Zhao, *ACS Nano*, 2010, **4**, 3187–3194.

7 J. M. Jeong, B. G. Choi, S. C. Lee, K. G. Lee, S. J. Chang, Y. K. Han, Y. B. Lee, H. U. Lee, S. Kwon, G. Lee, C. S. Lee and Y. S. Huh, *Adv. Mater.*, 2013, **25**, 6250–6255.

8 X. Lang, A. Hirata, T. Fujita and M. Chen, *Nat. Nanotechnol.*, 2011, **6**, 232–237.

9 L. Ji, Z. Lin, M. Alcoutlabi and X. Zhang, *Energy Environ. Sci.*, 2011, **4**, 2682–2699.

10 X. Liu, J. Zhang, X. Guo, S. Wang and S. Wu, *RSC Adv.*, 2012, **2**, 1650–1655.

11 W. Zhou, C. Cheng, J. Liu, Y. Y. Tay, J. Jiang, X. Jia, J. Zhang, H. Gong, H. H. Hng, T. Yu and H. J. Fan, *Adv. Funct. Mater.*, 2011, **21**, 2439–2445.

12 H. Wu, M. Xu, Y. Wang and G. Zheng, *Nano Research*, 2013, **6**, 167–173.

13 Q. Xiong, J. Tu, X. Xia, X. Zhao, C. Gu and X. Wang, *Nanoscale*, 2013, **5**, 7906–7912.

14 W. Zeng, F. Zheng, R. Li, Y. Zhan, Y. Li and J. Liu, *Nanoscale*, 2012, **4**, 2760–2765.

15 Y. Luo, J. Luo, J. Jiang, W. Zhou, H. Yang, X. Qi, H. Zhang, H. J. Fan, D. Y. W. Yu, C. M. Li and T. Yu, *Energy Environ. Sci.*, 2012, **5**, 6559–6566.

16 X. J. Zhu, Z. P. Guo, P. Zhang, G. D. Du, R. Zeng, Z. X. Chen, S. Li and H. K. Liu, *J. Mater. Chem.*, 2009, **19**, 8360–8365.

17 A. S. Arico, P. Bruce, B. Scrosatl and J.-m. Tarascon, *Nat. Mater.*, 2005, **4**, 366–378.

18 M. He, L. Yuan, X. Hu, W. Zhang, J. Shu and Y. Huang, *Nanoscale*, 2013, **5**, 3298–3305.

19 L. Ji, O. Toprakci, M. Alcoutlabi, Y. Yao, Y. Li, S. Zhang, B. Guo, Z. Lin and X. Zhang, *ACS Appl. Mater. Interfaces*, 2012, **4**, 2672–2679.

20 X. W. Lou, C. M. Li and L. A. Archer, *Adv. Mater.*, 2009, **21**, 2536–2539.

21 Q. Guo, Z. Zheng, H. Gao, J. Ma and X. Qin, *J. Power Sources*, 2013, **240**, 149–154.

22 J. Luo, J. Liu, Z. Zeng, C. F. Ng, L. Ma, H. Zhang, J. Lin, Z. Shen and H. J. Fan, *Nano Lett.*, 2013, **13**, 6136–6143.

23 J. Liu, J. Jiang, D. Qian, G. Tan, S. Peng, H. Yuan, D. Luo, Q. Wang and Y. Liu, *RSC Adv.*, 2013, **3**, 15457–15467.

24 S. Y. Kim, J. Hong, R. Kavian, S. W. Lee, M. N. Hyder, Y. Shao-Horn and P. T. Hammond, *Energy Environ. Sci.*, 2013, **6**, 888–898.

25 X. Huang, Z. Zeng, Z. Fan, J. Liu and H. Zhang, *Adv. Mater.*, 2012, **24**, 5979–6004.

26 C. Xu, B. Xu, Y. Gu, Z. Xiong, J. Sun and X. S. Zhao, *Energy Environ. Sci.*, 2013, **6**, 1388–1416.

27 M. Xu, T. Liang, M. Shi and H. Chen, *Chem. Rev.*, 2013, **113**, 3766–3798.

28 L. Chen, M. Zhang and W. Wei, *J. Nanomater.*, 2013, **2013**, 1–8.

29 L. Noerochim, J.-Z. Wang, D. Wexler, Z. Chao and H.-K. Liu, *J. Power Sources*, 2013, **228**, 198–205.

30 J. W. Lee, S. Y. Lim, H. M. Jeong, T. H. Hwang, J. K. Kang and J. W. Choi, *Energy Environ. Sci.*, 2012, **5**, 9889–9894.

31 G. Ji, B. Ding, Z. Sha, J. Wu, Y. Ma and J. Y. Lee, *Nanoscale*, 2013, **5**, 5965–5972.

32 W. Xiao, Z. Wang, H. Guo, X. Li, J. Wang, S. Huang and L. Gan, *Appl. Surf. Sci.*, 2013, **266**, 148–154.

33 G. Zhou, D. Wang, F. Li, L. Zhang, N. Li, Z. Wu, L. Wen, G. Lu and H. Cheng, *Chem. Mater.*, 2010, **22**, 5306–5313.

34 C. J. Song and L. X. Wen, *Small*, 2013, **9**, 1877–1893.

35 S. Ding, D. Luan, F. Y. Boey, J. S. Chen and X. W. Lou, *Chem. Commun.*, 2011, **47**, 7155–7157.

36 X. Zhu, Y. Zhu, S. Murali, M. D. Stoller and R. S. Ruoff, *ACS Nano*, 2011, **5**, 3333–3338.

37 J. Qu, Y. Yin, Y. Wang, Y. Yan, Y. Guo and W. Song, *ACS Appl. Mater. Interfaces*, 2013, **5**, 3932–3936.

38 G. Wang, X. Shen, J. Yao and J. Park, *Carbon*, 2009, **47**, 2049–2053.

39 B. Zhang, Q. B. Zheng, Z. D. Huang, S. W. Oh and J. K. Kim, *Carbon*, 2011, **49**, 4524–4534.

40 Z. Wu, W. Ren, L. Wen and H. Cheng, *ACS Nano*, 2010, **4**, 3187–3194.

41 A. Abouimrane, O. C. Compton, K. Amine and S. T. Nguyen, *J. Phys. Chem. C*, 2010, **114**, 12800–12804.

42 C. Wang, D. Li, C. O. Too and G. G. Wallace, *Chem. Mater.*, 2009, **21**, 2604–2606.

43 R. Wang, C. Xu, J. Sun, L. Gao and C. Lin, *J. Mater. Chem. A*, 2013, **1**, 1794–1801.

44 W. S. Hummers and R. E. Offeman, *J. Am. Chem. Soc.*, 1958, **80**, 1339.

45 T. Ishikawa and E. Matijevic, *Langmuir*, 1988, **4**, 26–31.

46 D. Lei, M. Zhang, B. Qu, L. Chen, Y. Wang, E. Zhang, Z. Xu, Q. Li and T. Wang, *Nanoscale*, 2012, **4**, 3422–3426.

47 R. Wang, C. Xu, J. Sun, Y. Liu, L. Gao and C. Lin, *Nanoscale*, 2013, **5**, 6960–6967.

48 J. Zhu, T. Zhu, X. Zhou, Y. Zhang, X. W. Lou, X. Chen, H. Zhang, H. H. Hng and Q. Yan, *Nanoscale*, 2011, **3**, 1084–1089.

49 W. Chen, S. Li, C. Chen and L. Yan, *Adv. Mater.*, 2011, **23**, 5679–5683.

50 M. Park, Y. Kang, G. Wang, S. Dou and H. Liu, *Adv. Funct. Mater.*, 2008, **18**, 455–461.

51 M. V. Reddy, T. Yu, C. H. Sow, Z. X. Shen, C. T. Lim, G. V. SubbaRao and B. V. R. Chowdari, *Adv. Funct. Mater.*, 2007, **17**, 2792–2799.

52 M. Mohamedi, S.-J. Lee, D. Takahashi, M. Nishizawa and T. Itoh, *Electrochim. Acta*, 2001, **46**, 1161–1168.

53 R. DemirCakan, Y. Hu, M. Antonietti, J. Maier and M. Titirici, *Chem. Mater.*, 2008, **20**, 1227–1229.

54 J. Lin, Z. Peng, C. Xiang, G. Ruan, Z. Yan, D. Natelson and J. M. Tour, *ACS Nano*, 2013, **7**, 6001–6006.

55 G. Xia, N. Li, D. Li, R. Liu, C. Wang, Q. Li, X. Lu, J. S. Spendelow, J. Zhang and G. Wu, *ACS Appl. Mater. Interfaces*, 2013, **5**, 8607–8614.

56 M. V. Reddy, G. V. Subba Rao and B. V. R. Chowdari, *J. Power Sources*, 2010, **195**, 5768–5774.

57 Y. Chen, B. Song, L. Lu and J. Xue, *Nanoscale*, 2013, **5**, 6797–6803.

58 J. Chen, X. Xia, J. Tu, Q. Xiong, Y. Yu, X. Wang and C. Gu, *J. Mater. Chem.*, 2012, **22**, 15056–15061.